

# Biaxial atomically resolved force microscopy based on a qPlus sensor operated simultaneously in the first flexural and length extensional modes

Cite as: Rev. Sci. Instrum. **92**, 043703 (2021); <https://doi.org/10.1063/5.0041369>

Submitted: 22 December 2020 • Accepted: 14 March 2021 • Published Online: 05 April 2021

 Dominik Kirpal,  Jinglan Qiu,  Korbinian Pürckhauer, et al.



View Online



Export Citation



CrossMark

## ARTICLES YOU MAY BE INTERESTED IN

[The qPlus sensor, a powerful core for the atomic force microscope](#)



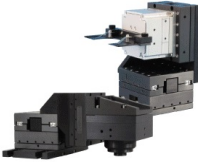
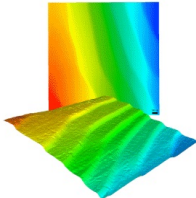
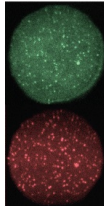
Review of Scientific Instruments **90**, 011101 (2019); <https://doi.org/10.1063/1.5052264>

[Combined atomic force microscope and scanning tunneling microscope with high optical access achieving atomic resolution in ambient conditions](#)

Review of Scientific Instruments **91**, 083701 (2020); <https://doi.org/10.1063/5.0013921>

[Low noise current preamplifier for qPlus sensor deflection signal detection in atomic force microscopy at room and low temperatures](#)

Review of Scientific Instruments **88**, 073702 (2017); <https://doi.org/10.1063/1.4993737>

	<p>Nanopositioning Systems</p> 	<p>Modular Motion Control</p> 	<p>AFM and NSOM Instruments</p> 	<p>Single Molecule Microscopes</p> 
---	--	--	---	--

# Biaxial atomically resolved force microscopy based on a qPlus sensor operated simultaneously in the first flexural and length extensional modes

Cite as: Rev. Sci. Instrum. 92, 043703 (2021); doi: 10.1063/5.0041369

Submitted: 22 December 2020 • Accepted: 14 March 2021 •

Published Online: 5 April 2021



View Online



Export Citation



CrossMark

Dominik Kirpal,<sup>1,a)</sup>  Jinglan Qiu,<sup>1,2</sup>  Korbinian Pürckhauer,<sup>1</sup>  Alfred J. Weymouth,<sup>1</sup>  Michael Metz,<sup>1</sup>   
and Franz J. Giessibl<sup>1</sup> 

## AFFILIATIONS

<sup>1</sup>Institute of Experimental and Applied Physics, University of Regensburg, D-93053 Regensburg, Germany

<sup>2</sup>College of Physics and Hebei Key Laboratory of Photophysics Research and Application, Hebei Normal University, Shijiazhuang, Hebei 050024, China

<sup>a)</sup> Author to whom correspondence should be addressed: [dominik.kirpal@physik.uni-r.de](mailto:dominik.kirpal@physik.uni-r.de)

## ABSTRACT

Frequency-modulation atomic force microscopy (AFM) with a qPlus sensor allows one to atomically resolve surfaces in a variety of environments ranging from low-temperature in ultra-high vacuum to ambient and liquid conditions. Typically, the tip is driven to oscillate vertically, giving a measure of the vertical force component. However, for many systems, the lateral force component provides valuable information about the sample. Measuring lateral and vertical force components simultaneously by oscillating vertically and laterally has so far only been demonstrated with relatively soft silicon cantilevers and optical detection. Here, we show that the qPlus sensor can be used in a biaxial mode with electrical detection by making use of the first flexural mode and the length extensional mode. We describe the necessary electrode configuration as well as the electrical detection circuit and compare the length extensional mode to the needle sensor. Finally, we show atomic resolution in ambient conditions of a mica surface and in ultra-high vacuum of a silicon surface. In addition to this, we show how any qPlus AFM setup can be modified to work as a biaxial sensor, allowing two independent force components to be recorded.

Published under license by AIP Publishing. <https://doi.org/10.1063/5.0041369>

## I. INTRODUCTION

Atomic force microscopy<sup>1</sup> (AFM) is an established method to investigate sample properties down to the atomic scale. Most AFM setups consist of a sharp tip attached to a cantilever. In dynamic AFM, the sensor acts as a damped driven harmonic oscillator excited at or near its resonance frequency and the tip-sample interaction influences this oscillation. The two most common dynamic modes are the amplitude modulation mode<sup>2</sup> (AM-AFM) and the frequency modulation mode<sup>3</sup> (FM-AFM). In AM-AFM, the sensor is driven with a constant frequency near the resonance frequency and a constant drive amplitude. The interaction between the tip and the sample influences the resonance frequency, and as a consequence, the oscillation amplitude changes. Information about the surface can be obtained by recording an amplitude map or using the amplitude as the feedback parameter for the tip-sample distance. In FM-AFM, the excitation follows the current resonance

frequency and the drive amplitude changes so that the oscillation amplitude remains constant. Surface information can be obtained from the shift of the resonance frequency (the frequency shift  $\Delta f$ ) and the drive amplitude is a measure of any additional damping. However, a tip oscillating perpendicular to the surface does not offer direct access to the lateral forces. These forces are of high interest for many experiments on the atomic scale such as lateral atomic manipulation.<sup>4</sup> Lateral forces can be accessed by oscillating the tip parallel to the surface [lateral force microscopy (LFM)]. This has been realized with silicon cantilevers by combining the flexural oscillation with a torsional mode<sup>5,6</sup> and for the qPlus sensor<sup>7,8</sup> by combining LFM with the STM feedback.<sup>9–12</sup> One less direct option to determine lateral forces is to integrate the FM-AFM signal vertically to determine the potential energy and then to take a lateral derivative to determine lateral forces.<sup>13</sup> However, this method requires a full three-dimensional dataset of  $\Delta f$  values of the observed area.

For the many AFM applications, various sensor types have been developed. The most commonly used types of sensors are micromachined silicon cantilevers with integrated tips.<sup>14</sup> These sensors offer the advantage that they can be produced in large numbers with well defined mechanical properties. The oscillation usually is detected with a laser beam reflected on the back of the cantilever and a photodiode detecting the laser reflection. A different type of sensor is the self-sensing sensor based on the piezoelectric effect<sup>15</sup> of quartz. Besides quartz tuning fork sensors,<sup>16</sup> the needle sensor<sup>17</sup> and the qPlus sensor<sup>7,8</sup> are well established. The electric detection method gives the advantage that a qPlus AFM microscope head is very compact and can be used without major adjustments in various environments ranging from air, liquid, ultra-high vacuum (UHV) to low

temperatures.<sup>8,18</sup> The high sensor stiffness  $k > 1$  kN/m has shown not to be a handicap when imaging soft samples, as demonstrated by nondestructively imaging biological samples.<sup>18</sup> Furthermore, the qPlus sensor enables using a wide range of tip materials. The ability to use conductive tip materials enables simultaneous AFM and STM measurements.

One approach to combine vertical and lateral movement of the tip was shown by Yamada *et al.*<sup>19</sup> using the second flexural mode of a qPlus sensor with a long tip. Increasing the tip length and the moment of inertia results in a shift of the node of the second flexural mode along the beam direction ( $x$ -direction).<sup>20</sup> If the node is at the free end of the oscillating cantilever, the amplitude in the  $z$ -direction becomes zero, but the curvature of the oscillating beam results in an arc shaped movement in the  $x$ -direction and negligible  $z$ -change. However, it is quite challenging to achieve the exact tip length needed.

Here, we present a different approach by using biaxial oscillation of the sensor. Beside the first flexural mode (1F-mode), we excite the length extensional mode (LE-mode), which means an oscillation in the beam direction. An established sensor using only the LE-mode is the needle sensor,<sup>21</sup> which is also made of quartz. This sensor type is a coupled oscillator consisting of two beams oscillating anti-parallel in the length extensional mode. Schematic drawings of the qPlus and needle sensor with an electrode configuration are displayed in Figs. 1(a) and 1(d). The electrode configuration of the qPlus sensor has to be adjusted for detecting both the flexural and the length extensional modes, as presented in Ref. 8, Fig. 8 [also see Fig. 1(g) in this work]. Here, we will include a detailed explanation and discussion of the required adjustments. During the project, a new design was developed, providing an optimized electrode configuration, which will be described in Sec. III and displayed in Fig. 2. Finally, the first qPlus LE-mode and combined 1F- and LE-mode measurements, performed with a single microscope in ultra-high vacuum (UHV) and ambient conditions, are shown.

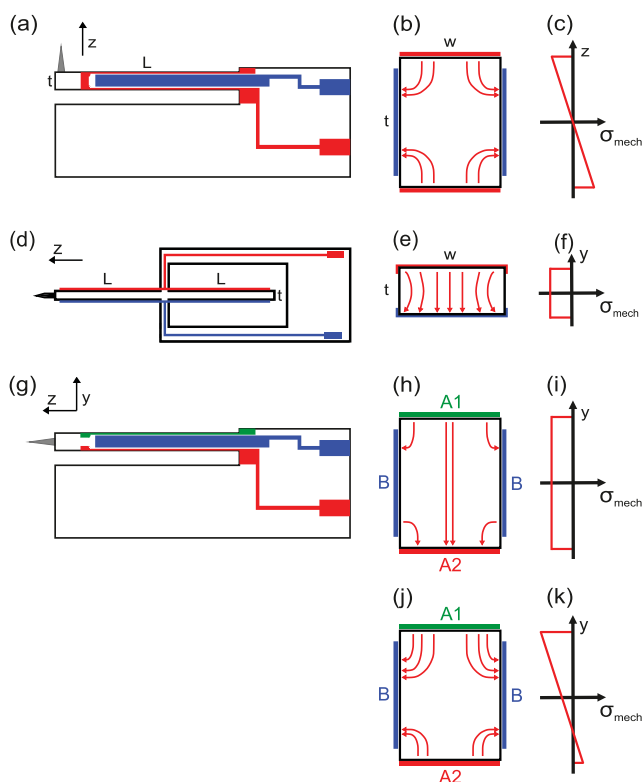


**FIG. 1.** Electrode configuration and electric fields resulting from strain due to a deflection of the beam. (a) A qPlus sensor optimized for using the first flexural mode. According to the stress (c) increasing linearly from the middle of the beam cross section in the first flexural mode, origin from the middle of the beam, the resulting electric field lines (b) go from the two opposite electrodes (A1 and A2) to the side electrodes (B) or reverse. For the needle sensor (d), the electric field (e) is almost homogeneous from one electrode to the opposing, according to a constant stress (f) in each cross section. In (g), the changed electrode configuration for LE detection of a qPlus sensor is displayed. The top [A1, see (h)] and bottom electrodes (A2) are separated, whereas the electrodes on the side of the beam remain connected. The electric field for single length extension is shown in (h) resulting from constant stress (i) in each cross section. For combined length extension and flexural deflection, a superposition of both situations is sketched in (j) and (k). The  $z$ -direction is defined as the tip direction perpendicular to the surface. Drawing adapted with permission from F. J. Giessibl, "The qPlus sensor, a powerful core for the atomic force microscope," *Rev. Sci. Instrum.* **90**, 011101 (2019). Copyright 2019 AIP Publishing LLC.

## II. THEORY

In this work, we combined the LE-mode of the single beam qPlus sensor with the 1F-mode to achieve tip oscillations in two dimensions. In the following text, the physical specifications and technical adjustments are described.

Each oscillating mode of a cantilever has its own physical properties. Higher flexural modes provide higher eigenfrequencies and much higher dynamic stiffnesses.<sup>22</sup> Although both modes can be excited and detected independently, the combined tip movement has to be considered when interpreting the tip-sample interaction.<sup>23,24</sup>

The properties of both the LE-mode and the 1F-mode are described in the following.

### A. Resonance frequency and stiffness of the modes

The cantilever is a damped, driven harmonic oscillator, vibrating with its resonance frequency, which is given for the first flexural mode by

$$f_{0,1F} = \frac{1}{2\pi} \sqrt{\frac{k_{1F}}{m_{\text{eff}}}}, \quad (1)$$

with the dynamic stiffness  $k_{1F}$  and the effective mass being approximately  $m_{\text{eff}} = 0.249 m$  of the total mass of the rectangular beam.<sup>25</sup>

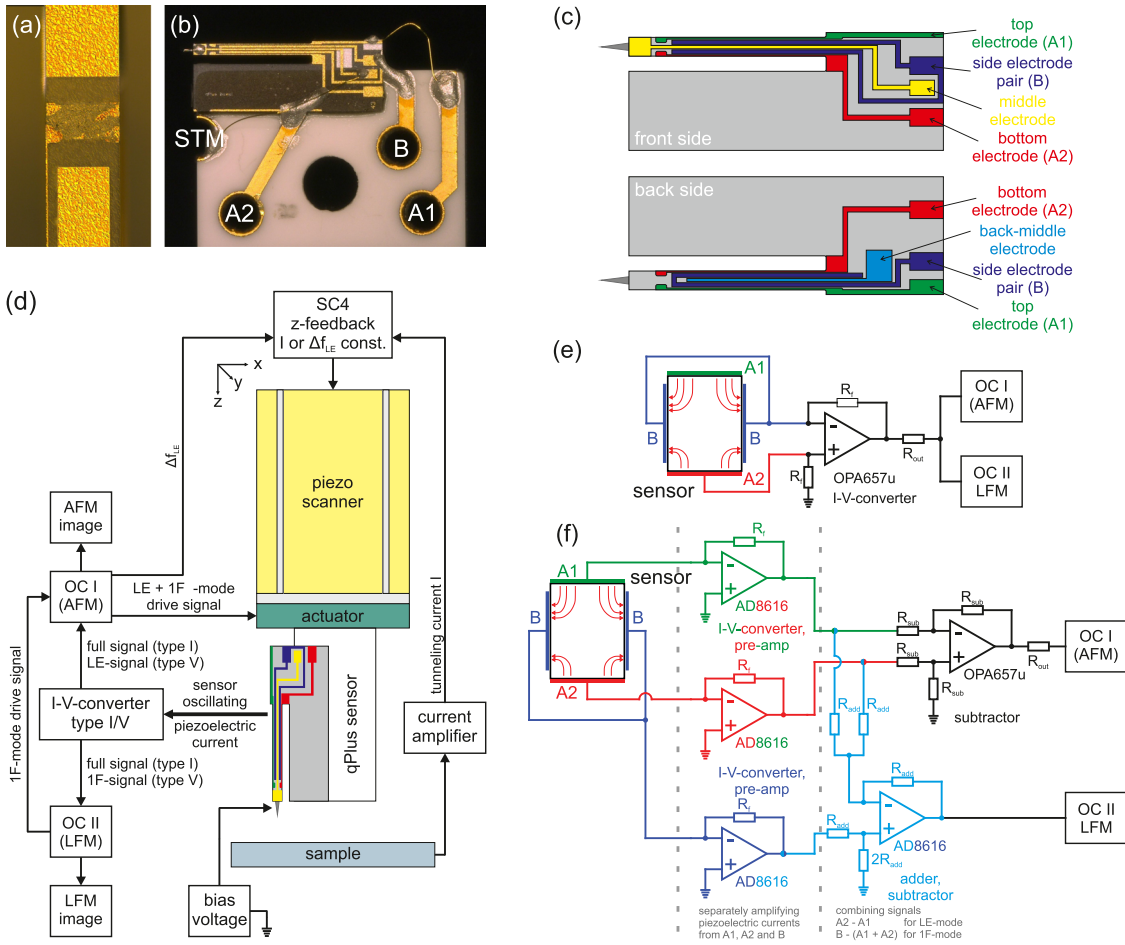


**FIG. 2.** Experimental setup for AFM and LFM with a qPlus sensor. (a) Locally removed gold electrode to separate A1 from A2. (b) Image of a biaxial qPlus sensor with four connections (A1, A2, B, and STM) with an attached Pt/Ir tip. (c) Schematic of the qPlus with a new designed electrode configuration with five different electrodes. (d) Schematic drawing of the microscope. Two OC modules are used to detect and excite one vibration mode each. They can be used for providing a constant drive signal or using a phase-locked-loop (PLL) for dynamic excitation following the current frequency as well as controlling the amplitude. (e) Schematic of the type I amplifier consisting of one single current to voltage converter. Only one of the top/bottom electrodes (here bottom electrode A2) as well as the side electrode pair (B) are detected differentially; the remaining electrode (here A1) is not connected. Image (f) shows the type V amplifier consisting of five I/V-converters. The signals of all three connections (A1, A2, and B) are separately amplified (green, red, and dark blue I/V-converters). The resulting signals are added or subtracted (black and light blue I/V-converters) and directed to the OC modules according to the oscillation mode.

The effective stiffness differs by +3% to the static load stiffness ( $k_{1F} = 1.03 k_{F,static}$ ),<sup>25</sup> which can be calculated by the dimensions of the cantilever,

$$k_{F,static} = \frac{Ewt^3}{4L^3}, \quad (2)$$

with Young's modulus<sup>20</sup>  $E = 7.87 \cdot 10^{10}$  N/m<sup>2</sup> for quartz and  $w$ ,  $t$ , and  $L$  being the width, thickness, and length of the beam, respectively [see Fig. 1(a)]. For the resonance frequency, it follows

$$f_{0,1F} = \frac{1.03}{2\pi} \sqrt{\frac{Ewt^3}{4L^3} \frac{4}{Lwt\rho}} \approx 0.162 \frac{t}{L^2} v_s, \quad (3)$$

with  $v_s = \sqrt{E/\rho} = 5449.6$  m/s being the speed of sound in quartz with density<sup>26</sup>  $\rho = 2.65$  g/cm<sup>3</sup>.

In the case of the length extensional mode, the base frequency and static stiffness are given by<sup>27</sup>

$$f_{0,LE} = \frac{v_s}{4L}, \quad (4)$$

$$k_{LE,static} = \frac{Ewt}{L}. \quad (5)$$

However, compared to the 1F-mode, the static and dynamic stiffnesses differ much more significantly for the LE-mode as the stress is constant over the beam length for static length extension but not

**TABLE I.** Dimensions, resonance frequencies  $f_0$ , and spring constants  $k$  of the used qPlus and the needle sensor. Note that the needle sensor consists of a coupled oscillator with two beams. The effective stiffness, therefore, is twice the stiffness of a single beam.<sup>21</sup> These values are calculated for sensors without a tip being attached. Especially, in the case of the qPlus S0.6, the frequency of the LE-mode can decrease by almost 50 % when attaching a tip. The dimensions of the needle sensor were taken from Ref. 21.

		$L$ ( $\mu\text{m}$ )	$L_e$ ( $\mu\text{m}$ )	$w$ ( $\mu\text{m}$ )	$t$ ( $\mu\text{m}$ )	$f_0$ (kHz)	$k_{\text{static}}$ (kN/m)	$k_{\text{dynamic}}$ (kN/m)	$S_{\text{theory}}$ ( $\mu\text{C}/\text{m}$ )
Needle sensor	(LE)	1340	1100	130	70	1016.7	1068.9	1318.7	60.949
qPlus S1.0	(1F)	2400	1900	130	214	32.8	1.813	1.868	3.024
	(LE)					567.7	9124.2	1431.0	29.390
qPlus S0.6	(1F)	1440	940	130	214	91.1	8.395	8.648	4.633
	(LE)					946.1	1520.4	1875.8	24.233

for the dynamic case, which is described in the supporting information of Ref. 27. The correction term for the  $n$ th LE-mode is given by

$$k_{\text{LE,dynamic}} = \frac{\pi^2(2n-1)^2}{8} k_{\text{LE,static}}. \quad (6)$$

This results in a 23 % higher stiffness for the base LE-mode compared to the static case.

qPlus sensors are available in various types, which mostly differ in dimension and electrode configuration. Here, we will concentrate on two of them. The two used versions have the same width and thickness,  $w = 130 \mu\text{m}$  and  $t = 214 \mu\text{m}$ , but have different lengths  $L_0 = 2400 \mu\text{m}$  (type qPlus S1.0 from Table I in Ref. 8) and  $L_{06} = 1440 \mu\text{m}$  ( $= 0.6 \cdot L_0$ ) (type qPlus S0.6 from Table I in Ref. 8). As a reference, we compare the resonance frequency and dynamic stiffness of the qPlus sensor to the needle sensor, which is a well established quartz length-extension resonator. The dimensions<sup>21</sup> are  $w = 130 \mu\text{m}$ ,  $t = 70 \mu\text{m}$ , and length  $L = 1340 \mu\text{m}$  for each arm. The calculated values are listed in Table I.

## B. Piezoelectric sensitivity

The self-sensing mechanism of the qPlus sensor, as well as other quartz tuning fork sensors or the needle sensor, is based on the piezoelectric effect. External stress of a piezoelectric material leads to polarization of the unit cells and consequently to an electric field. On the sensor surface, a thin gold film is deposited. The electric field induces a charge on this electrode, producing an alternating current when the beam oscillates. This current is measured after being converted to a voltage signal via a transimpedance amplifier (current to voltage converter). In Fig. 1, the electrode configuration and the electric field in a sensor are displayed for the first flexural mode of a qPlus sensor [(a)–(c)] and for the length extensional mode of the needle sensor [(d)–(f)], as well for combined flexural and length extensional deflection of the qPlus sensor [(g)–(k)]. A deflection perpendicular to the beam direction (flexural deflection) causes the same charges on the top and bottom electrodes [Fig. 1(b)] in contrast to the length extensional mode causing opposite charges [Fig. 1(e)].

The relation between oscillation amplitude  $A$  and generated charge  $q_{\text{el}}$  on the gold electrodes is given by sensitivity  $S$ . For the first flexural mode, it can be approximated according to Ref. 28,

$$S_{1F}^{\text{theory}} = \frac{q_{\text{el}}}{A} = 12d_{21}k \frac{L_e(L - L_e/2)}{t^2}, \quad (7)$$

with  $L_e$  being the length of the gold electrodes and  $d_{21} = 2.31 \text{ pC}/\text{m}$  being the transverse piezoelectric coupling coefficient<sup>15</sup> according to the cutting direction of the quartz crystal. This material constant is equal to the longitudinal coupling constant  $d_{11}$ .<sup>29</sup>

There are two caveats to the above calculation. The first is that this calculation refers to static deflection. For the two used qPlus sensor types, the difference is less than 6 % between the sensitivity for the static and dynamic calculation (for a more detailed calculation, see the [supplementary material](#)). The second is that the electric field lines are assumed to be parallel, which is not the case for our electrode configuration.<sup>21</sup> The field lines for the given electrode configurations and vibration modes are displayed in Figs. 1(b), 1(e), 1(h), and 1(j). On the sides of the cantilever as well as on the top and bottom sides are gold electrodes. In the original design, each electrode is connected to the electrode on the opposing side. Each electrode pair detects the opposite current to the neighboring pair when the sensor oscillates.

The sensitivity of the LE-mode is given by<sup>21</sup>

$$S_{\text{LE}} = Ewd_{11} \sin\left(\frac{\pi}{2L}L_e\right). \quad (8)$$

In the case of the needle sensor, the sensitivity is doubled due to the second beam. The calculated values are given in Table I.

## III. ELECTRODE CONFIGURATION AND AMPLIFIER DESIGN

The typical electrode configuration of a qPlus sensor is optimized for flexural detection. As mentioned in the previous part, the top and bottom electrodes [A1 and A2, see Figs. 1(h) and 1(j)] detect the same charges for flexural deflection and opposite charges for length extension. The qPlus sensor is designed for detection of the flexural mode. Therefore, the standard design is with both electrodes connected. To measure the length of the extensional mode, the top and bottom electrodes were disconnected as displayed in Figs. 1(g) and 1(h) (electrodes A1 and A2).

We realized this by using a spot welding mechanism and ripping off the connecting gold coating close to the free end of the beam. The electrode was connected to one pole of a few volts power supply ( $\sim 5$  to  $10 \text{ V}$ ) with sufficient current output (we used a DC power supply with  $15 \text{ V}$  and  $2 \text{ A}$  maximum output). A thin wire was connected to the other pole of the power supply (here, a  $50 \mu\text{m}$  thick copper wire). When the gold coating of the counter electrode was touched, a high current density occurred at the contact area. This

led to the gold attach to the wire and finally the layer around the contact point was ripped off. An image of a sensor beam with the gold electrode removed is shown in Fig. 2(a). Afterward, it was tested if the electrodes have been disconnected or a high-Ohmic contact remained. In that case, the sensor has to be replaced.

Furthermore, in course of the project, a new qPlus design was invented, whose electrode configuration was designed for detection of both flexural and length extensional modes. An image of the sensor is shown in Fig. 2(b), with a cut Pt/Ir-tip attached. The new electrode configuration is shown in Fig. 2(c). Here, the top (A1, green) and bottom (A2, red) electrodes are already disconnected by design. On the front side of the sensor, the side electrode (B) is divided by a small middle electrode connected to the end of the beam. This electrode can be used for connecting the tip for STM or electrical excitation. To avoid crosstalk between excitation and STM signal on the back side, the electrode is divided and an additional middle electrode is available, which however is not connected to the tip. This electrode on the back side is not relevant for the application of this paper, so it can be left unconnected or reconnected to the side electrode pair (B). This new sensor type only differs in the backside middle electrode from the sensors with the top-bottom connection removed (A1 separated from A2).

In Fig. 2(d), a schematic drawing of the microscope is shown. The amplified signal of the sensor is given to two oscillation controllers (OC) (OC4 module from SPECS GmbH), one for each oscillation mode. Each OC module is used to detect the resonance within a frequency window. They are also used to excite the sensor. For AM-AFM operation, this is done at a constant frequency and with a constant magnitude. For FM-AFM, the input is used as the feedback to follow the frequency and control the amplitude of the resonance. The OCs that we used offer an “add”-option, which adds the excitation signal of both modes to drive the actuator (a shaker piezo).

Both the LE- and the 1F-mode can be detected simultaneously by a differential current to voltage converter. A simple realization is to connect the side electrode pair (B) and one of the divided pair (e.g., A2) to the two amplifier inputs. The other input, here (A1), remains unconnected. A schematic drawing of this configuration is displayed in Fig. 2(e). This type I amplifier consists of a single current to voltage converter. The output resistor was installed to prevent railing of the operational amplifier (OPA657u, here  $R_{\text{add}} = 2.2 \text{ k}\Omega$ ).

An alternative amplifier setup has been designed to make use of both the A1 and A2 contacts. This type V amplifier consists of five current to voltage converters. We used two AD8616 as they provide two I/V-converters on one chip. The current of each separated electrode and the side pair are amplified by a single channel current converter [green, red, and dark blue I/V-converters in Fig. 2(f)]. For detection of the LE-mode, the signals of the separated electrodes are subtracted from each other:  $A2 - A1$  [black I/V-converter in Fig. 2(f)]. For the 1F-mode detection, those signals are added again and subtracted from the side electrode signal:  $B - (A2 - A1)$  [light blue I/V-converter in Fig. 2(f)]. The amplifiers are described in Ref. 30.

As well as AFM and LFM, the setup allows tunneling current detection with a separate current amplifier connected to the middle electrode at the front side of the qPlus sensor [yellow in Fig. 2(c)].

## IV. RESULTS AND DISCUSSION

We performed FM-AFM in the LE mode (LE-FM-AFM) and lateral force microscopy in both AM and FM modes using the 1F mode (1F-AM-LFM and 1F-FM-LFM, respectively). The experimental part of this project consists of three parts. First, we show the capability of this qPlus setup to achieve atomic resolution in LE-FM-AFM in ambient conditions. Second, we combined LE-FM-AFM and 1F-AM-LFM to realize simultaneous biaxial measurements on mica. However, it was difficult to perform 1F-FM-LFM in ambient conditions. Therefore, we moved to UHV to demonstrate simultaneous LE-FM-AFM, 1F-FM-LFM, and STM results of Si(111)- $7 \times 7$ . Due to thermal drift, calibration of the LE amplitude did not provide reproducible results in ambient conditions. Therefore, we can only give a rough estimation of the range being  $A_{LE} \approx 100\text{--}500 \text{ pm}$ . An exact determination using the STM feedback was only performed for the UHV measurements.

### A. LE-FM-AFM measurements in ambient conditions

In this part, we investigated the well-known sample systems such as potassium bromide<sup>31–33</sup> [KBr(100), bought from MaTek] and muscovite mica<sup>34</sup> (V1 grade, purchased from Plano GmbH). KBr crystallizes in the rock salt structure and was cleaved with a razor blade. Typically, the surface shows many steps with varying heights from single atomic layers up to some nanometers, and the terraces have a size up to several 100 nanometers. Figure 3(a) shows a  $2 \times 2 \mu\text{m}^2$  KBr(100) surface. Several terraces and monoatomic steps can be observed.

The muscovite mica sample was cleaved with scotch tape resulting in an atomically flat and clean surface without any steps. In Fig. 3(b), an  $8 \times 8 \text{ nm}^2$  area is displayed revealing the atomic honeycomb structure. To compensate the drift, the scanning was performed in a quasi-constant-height mode, which means that the height feedback is too slow to follow the surface structure. Atomic resolution, therefore, can be observed in the frequency shift image. Both the step structures of KBr(100) and the atomic resolution of mica demonstrate the capability of the qPlus sensor to perform

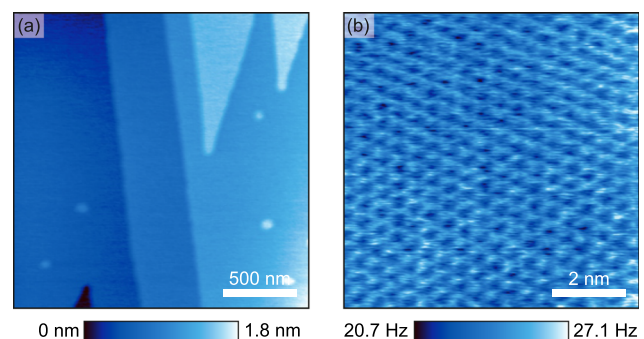


**FIG. 3.** LE-AFM scans of KBr (a) and mica (b) in ambient conditions. The qPlus S1.0 was equipped with a sapphire tip. The resonance frequency is  $f_{0,LE} = 466 \text{ kHz}$ . (a)  $2 \times 2 \mu\text{m}^2$  large KBr(100) surface. Large terraces and monoatomic steps can be observed. The frequency shift setpoint is  $\Delta f = 10 \text{ Hz}$ . (b) Atomic resolution of the mica surface on an  $8 \times 8 \text{ nm}^2$  frequency shift image. The honeycomb structure of mica can be observed. An average frequency shift of  $\langle \Delta f \rangle = 24 \text{ Hz}$  is observed in the quasi-constant-height mode.

AFM measurements in the length extensional mode, which lays the foundation for the next biaxial measurements.

### B. Combined LE-FM-AFM and 1F-AM-LFM measurements in ambient conditions

As a next step, the first flexural mode was excited additionally. At imaging distance ( $\Delta f_{LE}$  feedback of a few Hz), we performed a frequency sweep of the first flexural mode (lateral oscillation). However, no resonance peak was observed. For this reason, we decided to excite the 1F-LFM-mode at its free resonance frequency (as free resonance frequency or free amplitude, we consider the resonance frequency or amplitude when the sensor is far away from the sample) with constant drive amplitude and the resulting cantilever oscillation amplitude was measured (1F-AM-LFM). When the tip was distant from the surface, the amplitude was set to 100 pm. At imaging distance, the amplitude dropped to a few tens of picometers. The atomic structure of the mica sample can be seen in the frequency shift image of the LE-mode shown in Fig. 4(a). The corresponding amplitude and phase images of the 1F-AM-LFM mode in (b) and (c) also show a structure following the atomic pattern. In order to compare the structures in the  $\Delta f_{LE}$  and  $A_{1F}$  channels, we overlaid both images by a lattice with the lattice points being arranged according to the  $\Delta f_{LE}$  image. The amplitude  $A_{1F}$  is lower at the atom positions than between them. This indicates higher dissipation at the surface atom positions than between them. (As explained above, the sensor showed no resonance curve in the 1F-mode when close to the surface. Therefore, the LFM amplitude contrast cannot be explained by a shift of the resonance frequency.)

An interesting question is how both modes influence each other. For investigation, we took several  $6 \times 6 \text{ nm}^2$  images and changed the excitation strength of the LFM mode. In Fig. 5, the  $\Delta f_{LE}$  [Figs. 5(a), 5(c), and 5(e)] and  $A_{1F}$  [Figs. 5(b), 5(d), and 5(f)] images are compared. The setpoints (free amplitude) of the LFM amplitudes are 350 pm [Fig. 5(b)], 250 pm [Fig. 5(d)], and 100 pm [Fig. 5(f)]. When decreasing the LFM amplitude, the structure in  $\Delta f_{LE}$  images changes from a very unclear and barely visible stripe pattern in Fig. 5(c) to clear atomic contrast in Fig. 5(e). However, atomic structures can be observed in all LFM images. The results show that if the lateral amplitude is too high, atomic resolution in  $\Delta f_{LE}$  images cannot be observed.

In Ref. 23, Kawai *et al.* discuss the mutual influence of the vertical and lateral modes using a torsional LFM mode in UHV conditions. They state that as long as the LFM amplitude is small compared to the surface features, the AFM signal is expected to be the same with and without oscillation. When the LFM oscillation starts to get larger compared to the size of the surface features, the AFM signal will be an average over the tip motion.

### C. Combined LE-FM-AFM, 1F-FM-LFM, and STM measurements in UHV conditions

Considering the difficulties of performing 1F-FM-LFM in ambient conditions, we transferred our microscope to UHV. There, it was easier to control the LFM mode with the tip in the interaction range to the surface, and thus, it was possible to realize 1F-FM-LFM measurements. We prepared a Si(111)- $7 \times 7$  surface by a standard cleaning procedure of flashing up to  $1350^\circ\text{C}$  for a few seconds with an electron beam heater while keeping the pressure during heating

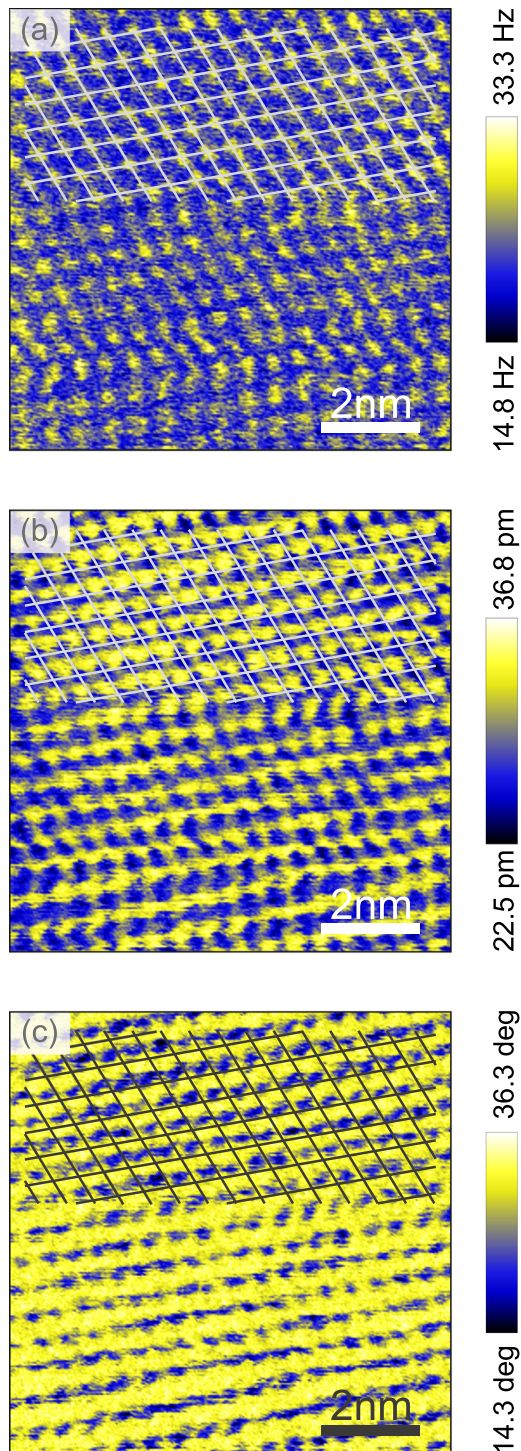


**FIG. 4.** Atomically resolved mica surface. (a) The LE-mode frequency shift and (b)/(c) the corresponding AM-LFM amplitude and phase. The overlaying grid marks the positions of the scanned atoms. In the LFM-amplitude image, it can be observed that the positions of the atom centers show the lowest amplitude and, therefore, the highest dissipation. (c) The atomic pattern in the 1F-AM-LFM phase. Scan parameters:  $\Delta f_{LE} = 23 \text{ Hz}$  and  $A_{1F,free} = 100 \text{ pm}$ .

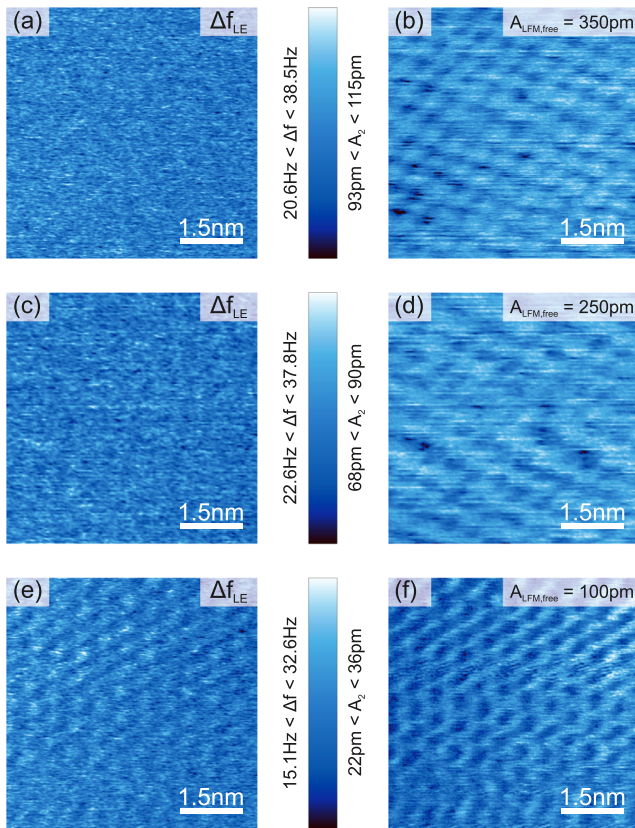


**FIG. 5.** Images of simultaneous LE-FM-AFM and 1F-AM-LFM as a function of excitation of the LFM mode. [(a), (c), and (e)] The LE frequency shift  $\Delta f_{LE}$ . The corresponding amplitude images of the LFM modes are at free amplitudes of (b) 350 pm, (d) 250 pm, and (f) 100 pm. The atomic structure can be observed for all 1F-amplitude images, however, only in the frequency shift in (e). We used a qPlus S0.6 with W-tip,  $f_{0,LE} = 453.7$  kHz, and  $f_{0,1F} = 43.7$  kHz.

below  $3 \times 10^{-9}$  mbar. The measurement was taken in quasi-constant height with a slow STM feedback.

Figure 6 shows the atomic resolution of Si(111)- $7 \times 7$  reconstruction in the tunneling current (a), length extensional AFM frequency shift (b), and first flexural LFM frequency shift (c) channels. Since the positive bias was added to the tip, the STM image of Fig. 6 shows the occupied sample states. The 12 protrusions in one  $7 \times 7$  unit cell (marked by the overlaid lattice and the red dots) correspond to the 12 Si adatoms. By comparing the three images, it is easy to find that the protrusions in the length extensional AFM frequency shift image are also located on Si adatoms, the same as in STM. The positive frequency shift values in Fig. 6(b) indicate less attraction over the adatoms.

Typically, LFM images show a more complex structure<sup>35,36</sup> as shown in Fig. 6(c). When imaging the lateral force gradient of a repulsive feature, a negative frequency shift at the potential center surrounded by positive frequency shift is expected. The LFM frequency shift displayed in Fig. 6(c) shows the expected shape (compared to the attractive feature described in FIG. 1 in Ref. 36). However, we observe a lateral shift of roughly 0.2 nm ( $\pm 0.1$  nm) from

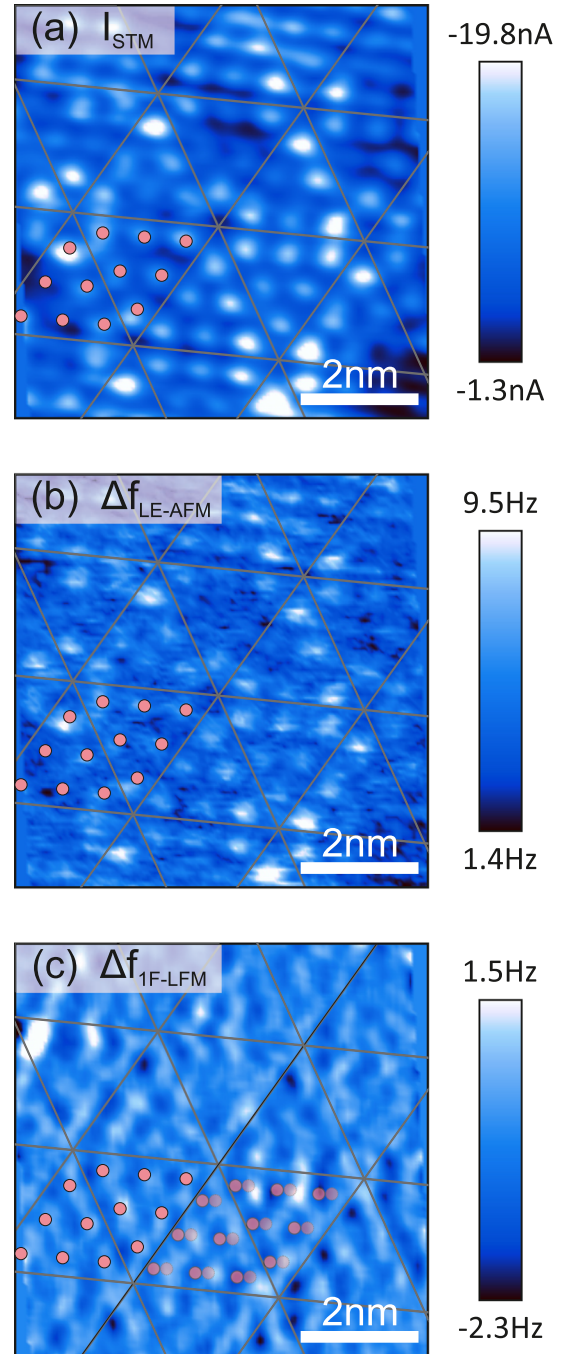


**FIG. 6.**  $7 \times 7$  nm<sup>2</sup> sector of a Si(111)- $7 \times 7$  surface showing atomic resolution in current (a),  $\Delta f_{LE-AFM}$  (b), and  $\Delta f_{1F-LFM}$  (c). All images are recorded simultaneously in the quasi-constant height mode. Images (a) and (c) are processed with a Gaussian smooth. The overlaid lines mark the  $7 \times 7$  supercells and the red dots mark the 12 Si adatoms. In image (c), a set of adatoms (transparent, dotted circle) is displayed with an additional set (transparent, solid circle) shifted by 0.16 nm, which matches with the  $\Delta f$  minima. We used a qPlus S1.0 with a Pt/Ir tip. The resonance frequencies and estimated spring constants are  $f_{0,LE} = 424.465$  kHz,  $k_{LE} = 567.7$  kN/m,  $f_{0,1F} = 27.441$  kHz, and  $k_{1F} = 1.8$  kN/m. The amplitude setpoints of both the modes were  $A_{LE} = A_{1F} = 100$  pm. The bias is 300 mV.



the adatom positions as identified in the STM image in the fast scan direction that we cannot fully explain.

## V. SUMMARY AND OUTLOOK

In this work, we showed that it is possible to excite and detect the oscillation of the length extensional mode of the qPlus sensor. This mode is capable of achieving atomic resolution in UHV and ambient conditions. Furthermore, atomic resolution was achieved in biaxial length extensional FM-AFM and flexural AM-LFM simultaneously.

We presented the modifications required to perform biaxial AFM on a qPlus setup. This combines the advantage of LFM with AFM and the compact setup of a qPlus atomic force microscope. This combination can be valuable, especially for low temperature microscopes where a compact design is preferred.

## AUTHORS' CONTRIBUTION

D.K. and J.Q. contributed equally to this work.

## SUPPLEMENTARY MATERIAL

See the [supplementary material](#) for the calculations of the dynamic and static stiffnesses of the first flexural mode.

## ACKNOWLEDGMENTS

We acknowledge the German Research Foundation (Grant No. SFB 1277, Project No. A02) for their support and thank Anja Merkel for helping to build the experimental setup and Alexander Liebig and Oliver Gretz for the fruitful discussions. Furthermore, we acknowledge the funding of Faculty Study Abroad Programs provided by Hebei Normal University for making this collaboration possible.

## DATA AVAILABILITY

The data that support the findings of this study are available from the corresponding author upon reasonable request.

## REFERENCES

- 1 G. Binnig, C. F. Quate, and C. Gerber, "Atomic force microscope," *Phys. Rev. Lett.* **56**, 930–933 (1986).
- 2 Y. Martin, C. C. Williams, and H. K. Wickramasinghe, "Atomic force microscope-force mapping and profiling on a sub 100-Å scale," *J. Appl. Phys.* **61**, 4723–4729 (1987).
- 3 T. R. Albrecht, P. Grütter, D. Horne, and D. Rugar, "Frequency modulation detection using high-Q cantilevers for enhanced force microscope sensitivity," *J. Appl. Phys.* **69**, 668 (1991).
- 4 O. Custance, R. Perez, and S. Morita, "Atomic force microscopy as a tool for atom manipulation," *Nat. Nanotechnol.* **4**, 803–810 (2009).
- 5 G. Meyer and N. M. Amer, "Simultaneous measurement of lateral and normal forces with an optical-beam-deflection atomic force microscope," *Appl. Phys. Lett.* **57**, 2089–2091 (1990).
- 6 E. Arima, H. Wen, Y. Naitoh, Y. J. Li, and Y. Sugawara, "Development of low temperature atomic force microscopy with an optical beam deflection system capable of simultaneously detecting the lateral and vertical forces," *Rev. Sci. Instrum.* **87**, 093113 (2016).
- 7 F. J. Giessibl, "High-speed force sensor for force microscopy and profilometry utilizing a quartz tuning fork," *Appl. Phys. Lett.* **73**, 3956 (1998).
- 8 F. J. Giessibl, "The qPlus sensor, a powerful core for the atomic force microscope," *Rev. Sci. Instrum.* **90**, 011101 (2019).
- 9 S. P. Jarvis, H. Yamada, K. Kobayashi, A. Toda, and H. Tokumoto, "Normal and lateral force investigation using magnetically activated force sensors," *Appl. Surf. Sci.* **157**, 314–319 (2000).
- 10 O. Pfeiffer, R. Bennewitz, A. Baratoff, E. Meyer, and P. Grütter, "Lateral-force measurements in dynamic force microscopy," *Phys. Rev. B* **65**, 161403 (2002).
- 11 F. J. Giessibl, M. Herz, and J. Mannhart, "Friction traced to the single atom," *Proc. Natl. Acad. Sci. U. S. A.* **99**, 12006–12010 (2002).
- 12 T. Seeholzer, O. Gretz, F. J. Giessibl, and A. J. Weymouth, "A Fourier method for estimating potential energy and lateral forces from frequency-modulation lateral force microscopy data," *New J. Phys.* **21**, 083007 (2019).
- 13 M. Ternes, C. P. Lutz, C. F. Hirjibehedin, F. J. Giessibl, and A. J. Heinrich, "The force needed to move an atom on a surface," *Science* **319**, 1066–1069 (2008).
- 14 O. Wolter, "Micromachined silicon sensors for scanning force microscopy," *J. Vac. Sci. Technol., B* **9**, 1353 (1991).
- 15 C. J. Chen, *Introduction to Scanning Tunneling Microscopy* (Oxford University Press, Inc., 1993).
- 16 P. Günther, U. C. Fischer, and K. Dransfeld, "Scanning near-field acoustic microscopy," *Appl. Phys. B: Photophys. Laser Chem.* **48**, 89–92 (1989).
- 17 K. Bartzke *et al.*, "The needle sensor—a micromechanical detector for atomic force microscopy," *Int. J. Optoelectron.* **8**, 669 (1993).
- 18 K. Pürckhauer, A. J. Weymouth, K. Pfeffer, L. Kullmann, E. Mulvihill, M. P. Krahn, D. J. Müller, and F. J. Giessibl, "Imaging in biologically-relevant environments with AFM using stiff qPlus sensors," *Sci. Rep.* **8**, 9330 (2018).
- 19 Y. Yamada, T. Ichii, T. Utsunomiya, and H. Sugimura, "Simultaneous detection of vertical and lateral forces by bimodal AFM utilizing a quartz tuning fork sensor with a long tip," *Jpn. J. Appl. Phys., Part 1* **58**, 095003 (2019).
- 20 R. C. Tung, T. Wutscher, D. Martinez-Martin, R. G. Reifengerger, F. Giessibl, and A. Raman, "Higher-order eigenmodes of qPlus sensors for high resolution dynamic atomic force microscopy," *J. Appl. Phys.* **107**, 104508 (2010).
- 21 F. J. Giessibl, F. Pielmeier, T. Eguchi, T. An, and Y. Hasegawa, "Comparison of force sensors for atomic force microscopy based on quartz tuning forks and length-extensional resonators," *Phys. Rev. B* **84**, 125409 (2011).
- 22 H.-J. Butt and M. Jaschke, "Calculation of thermal noise in atomic force microscopy," *Nanotechnology* **6**, 1 (1995).
- 23 S. Kawai, T. Glatzel, S. Koch, B. Such, A. Baratoff, and E. Meyer, "Ultrasensitive detection of lateral atomic-scale interactions on graphite (0001) via bimodal dynamic force measurements," *Phys. Rev. B* **81**, 085420 (2010).
- 24 H. Ooe, D. Kirpal, D. S. Wastl, A. J. Weymouth, T. Arai, and F. J. Giessibl, "Amplitude dependence of image quality in atomically-resolved bimodal atomic force microscopy," *Appl. Phys. Lett.* **109**, 141603 (2016).
- 25 J. Melcher, S. Hu, and A. Raman, "Equivalent point-mass models of continuous atomic force microscope probes," *Appl. Phys. Lett.* **91**, 053101 (2007).
- 26 K. A. Hofmann, *Anorganische Chemie*, 21st ed. (Springer-Verlag, 1973), p. 865.
- 27 Y. Sugimoto and J. Onoda, "Force spectroscopy using a quartz length-extension resonator," *Appl. Phys. Lett.* **115**, 173104 (2019).
- 28 F. J. Giessibl, "Atomic resolution on Si(111)-(7 × 7) by noncontact atomic force microscopy with a force sensor based on a quartz tuning fork," *Appl. Phys. Lett.* **76**, 1470 (2000).
- 29 R. W. Ward, "The constants of alpha quartz," in *38th Annual Symposium on Frequency Control, 29 May-1 June 1984* (IEEE, 2005).
- 30 F. Huber and F. J. Giessibl, "Low noise current preamplifier for qPlus sensor deflection signal detection in atomic force microscopy at room and low temperatures," *Rev. Sci. Instrum.* **88**, 073702 (2017).
- 31 F. J. Giessibl and G. Binnig, "Investigation of the (001) cleavage plane of potassium bromide with an atomic force microscope at 4.2 K in ultra-high vacuum," *Ultramicroscopy* **42-44**, 281–289 (1992).
- 32 D. S. Wastl, A. J. Weymouth, and F. J. Giessibl, "Optimizing atomic resolution of force microscopy in ambient conditions," *Phys. Rev. B* **87**, 245415 (2013).

<sup>33</sup>D. J. Kirpal, K. Pürckhauer, A. J. Weymouth, and F. J. Giessibl, “Ion mobility and material transport on KBr in air as a function of the relative humidity,” *Beilstein J. Nanotechnol.* **10**, 2084 (2019).

<sup>34</sup>T. Fukuma, K. Kobayashi, K. Matsushige, and H. Yamada, “True atomic resolution in liquid by frequency-modulation atomic force microscopy,” *Appl. Phys. Lett.* **87**, 22–25 (2005).

<sup>35</sup>S. Kawai, N. Sasaki, and H. Kawakatsu, “Direct mapping of the lateral force gradient on Si(111)-(7 × 7),” *Phys. Rev. B* **79**, 195412 (2009).

<sup>36</sup>A. J. Weymouth, E. Riegel, S. Matencio, and F. J. Giessibl, “Evaluating the potential energy landscape over single molecules at room temperature with lateral force microscopy,” *Appl. Phys. Lett.* **112**, 181601 (2018).